Research Article Vol. 31, No. 20 / 25 Sep 2023 / Optics Express 33565
Optics EXPRESS

Simultaneous spectral differentiation of multiple fluorophores in super-resolution imaging using a glass phase plate

SANDUNI I. FERNANDO,[1] JASON T. MARTINEAU,[1] ROBERT J. HOBSON,[2] THIEN N. VU,[2] BRIAN BAKER,[3] BRIAN D. MUELLER,[2] RAJESH MENON,[4] ERIK M. JORGENSEN,[2] AND JORDAN M. GERTON[1,*]

[1] *University of Utah Department of Physics and Astronomy, 201 James Fletcher Bldg. 115 S. 1400 E Salt Lake City, UT 84112-0830, USA*
[2] *University of Utah School of Biological Sciences, 257 South 1400 East Salt Lake City, Utah 84112, USA*
[3] *University of Utah Nanofab 36 S. Wasatch Drive, SMBB Room 2500 Salt Lake City, UT 84112, USA*
[4] *University of Utah Department of Electrical and Computer Engineering 50 S. Central Campus Drive, MEB Room 2110 Salt Lake City, UT 84112, USA*
[*] *jordan.gerton@utah.edu*

Abstract: By engineering the point-spread function (PSF) of single molecules, different fluorophore species can be imaged simultaneously and distinguished by their unique PSF patterns. Here, we insert a silicon-dioxide phase plate at the Fourier plane of the detection path of a wide-field fluorescence microscope to produce distinguishable PSFs (X-PSFs) at different wavelengths. We demonstrate that the resulting PSFs can be localized spatially and spectrally using a maximum-likelihood estimation algorithm and can be utilized for hyper-spectral super-resolution microscopy of biological samples. We produced superresolution images of fixed U2OS cells using X-PSFs for dSTORM imaging with simultaneous illumination of up to three fluorophore species. The species were distinguished only by the PSF pattern. We achieved ~21-nm lateral localization precision (FWHM) and ~17-nm axial precision (FWHM) with an average of 1,800 - 3,500 photons per PSF and a background as high as 130 - 400 photons per pixel. The modified PSF distinguished fluorescent probes with ~80 nm separation between spectral peaks.

1. Introduction

Single Molecule Localization Microscopy (SMLM) [1] has dramatically transformed biological fluorescence microscopy over the past two decades. SMLM techniques [2] like PALM [3–6], STORM [7–9], and PAINT [10,11] have overcome the optical diffraction limit imposed by traditional light microscopes and have produced sharper images and videos of intracellular processes [12]. Initially, SMLM techniques were applied to single fluor species [3,6,8], and multi-color imaging was accomplished by separating different emission spectra either in time (serial excitation/collection) [13], which slows acquisition speeds, or in space (dedicated fields of view on a camera and a system of spectral filters) [14–16], which results in the loss of signal. One approach to improve the utility of SMLM techniques is to modify or engineer the point-spread function of the collected fluorescence emission, which has enabled, for example, increases in axial localization precision [1,14,17–22] and spectral identification of fluorophore emission [16,23–30]. The PSFs are engineered by introducing an additional optic such as a grating, phase ramp, or phase mask (created by a liquid crystal spatial light modulator, or dielectric) at the Fourier plane of the detection path [4,19,31]. Maximum likelihood estimation [32] and deep learning algorithms [33–36] have been used to localize the engineered PSFs with a precision of

#499929 https://doi.org/10.1364/OE.499929
Journal © 2023 Received 12 Jul 2023; revised 5 Sep 2023; accepted 10 Sep 2023; published 21 Sep 2023

Optics EXPRESS

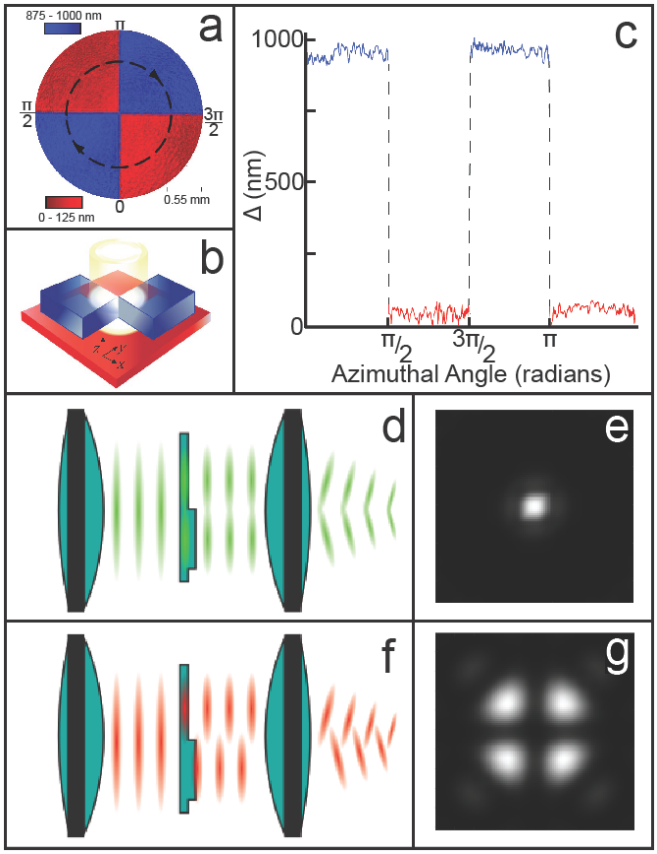

Fig. 1. Geometry and working principle of the phase plate. a) A schematic of the phase plate. The blue regions are fused silica depositions on top of a thin glass plate (red). The emission light is incident on the phase plate at its center as indicated by the bright spot. b) A color-coded thickness map of an approximately 2-mm section of the phase plate's center in the *x*-*y* plane measured by a Twyman-Green interferometer, as a thickness difference from a nominal zero. c) The thickness profile (z) along the dashed black circle. d) to g) The working principle of the phase plate. Panels (d) and (f) show how the phase plate affects fluorescence light of two wavelengths corresponding to 2π and π phase shifts respectively.). (e) and (g) show the corresponding simulated PSFs

tens of nanometers. PSF engineering has yielded both wavelength and position-dependent PSFs [37] and may thus eliminate the need to couple other imaging modalities such as spectrometers and emission filters to distinguish spectra. In addition, engineered PSFs have the potential to distinguish between highly overlapping spectra that cannot otherwise be separated using emission filters. For example, a single laser could be used to excite different proteins tagged with only red dyes which could be distinguished by their unique PSFs [38]. Spectral unmixing [39], biplane imaging [5], and spectral multiplexing [40] are compatible and complementary alternatives to PSF engineering.

In this paper, we modify the PSF in a spectrum-dependent manner using a single phase-mask created by a customized glass phase plate (Fig. 1) and demonstrate simultaneous (one-shot) nm-scale spatial localization and spectral differentiation of up to three fluorophore species. The modified PSF is referred to as an "X-PSF" based on its distinctive shape, and the customized phase plate the "X-PP" as explained below. By inserting the X-PP into the Fourier plane of a commercial

Optics EXPRESS

fluorescence microscope, we demonstrate spectral differentiation under simultaneous illumination, and successfully image and identify microtubules, mitochondria and ds-DNA in a fixed cell. Compared to some other PSF-engineering approaches, the X-PP is easy to manufacture at scale using standard masking and chemical vapor deposition technology. Furthermore, the X-PP yields a compact PSF that minimizes overlap between different regions of interest and helps prevent deterioration of the signal-to-noise ratio from spreading the photons over many camera pixels. Further, the X-PP does not limit fluorescence detection to a single narrow-width detection band so the photon budget will be maximized. Our approach, which utilizes a maximum-likelihood estimation algorithm, enables concurrent fitting of the position (in 3D) and wavelength of each localized fluor.

2. Methods

2.1. Working principle

We can enhance the capability of identifying fluorophore species by engineering a phase mask to produce maximally distinctive PSFs on a camera for different emission spectra. A glass phase plate having different thickness regions introduces a wavelength-dependent phase shift as light passes through the different regions. As a result, PSFs for fluorescence emission have a distinctive wavelength-sensitive pattern. Our phase plate geometry consists of four quadrants, with each diagonal pair having the same thickness, as shown in Fig. 1(a). Figure 1(d) and (f) depict collimated light propagating through a simplified model of the phase plate. As collimated fluorescence passes through the phase plate, the light passing through the thin and thick quadrants accumulate different phase shifts, ϕ. The phase shift incurred by a thickness difference Δ is $\phi = k(n_p - n_a)\Delta$, where n_p and n_a are refractive indices of glass and air, and $k = 2\pi/\lambda$ is the wave number. When ϕ is an even multiple of π, the wavefront passing through the phase plate interferes constructively and produces a PSF similar to an Airy disk as shown in Fig. 1(e). When ϕ is an odd multiple of π, the wavefronts interfere destructively at the center of the PSF, creating a cross-shaped null as shown in Fig. 1(g). Hereafter, we refer to the PSF patterns in panels (e) and (g) as the canonical forms of the X-PSF. For other values of ϕ, the observed PSF is a superposition of these two patterns. Thus, for two given wavelengths, maximally distinct X-PSFs can be obtained by choosing Δ appropriately. For this diagonally symmetric thickness configuration, the intensity migrates along the diagonals when an emitter's depth coordinate (z) varies from negative to positive with respect to the focal plane, as shown in the Supplement 1. Thus, we refer to this PSF as the "X-PSF", and the phase plate as the "X-phase plate" (X-PP).

For the work described here, we chose $\Delta = 960$ nm, for which the canonical forms span the entire range of the visible spectrum with $\phi = 2\pi$ at $\lambda = 442$ nm and $\phi = \pi$ at $\lambda = 884$ nm. We implemented phase plates with similar geometry but with thickness differences of 330, 660, and 720 nm, which had the capability to distinguish spectra but the 960-nm thick phase plate out-performed others in both spatial and spectral localizability. We measured the surface profile of the phase plate using phase-shifting interferometry with a Twyman-Green setup [41,42] as shown in Fig. 1(b-c). The quadrants indicated in blue measured $\Delta = 960 \pm 20$ nm thicker than those in red.

2.2. Optical setup

The X-PP was manufactured using a plasma-enhanced chemical vapor deposition process. More details about the design and fabrication of the X-PP and its mount can be found in the supplementary material (see Supplement 1). Figure 2(a) shows a greatly simplified diagram of the detection arm of our microscope. Two parallel bundles of rays are depicted, which pass through the X-PP from two different emitters on the sample. The parallel bundles of rays overlap at the Fourier plane. It is important to place the X-PP at this location, as this renders the X-PSFs

Optics EXPRESS

translationally invariant with respect to both the sample and image (camera) planes [22], [40]. We conducted the experiments using a Vutara 352 commercial microscope with the optical setup depicted in Fig. 2(b). The microscope had a silicon objective with a numerical aperture NA = 1.3. We incorporated the X-PP at the last Fourier plane of the detection path. The phase plate was manually adjusted to be within ~5 mm of the Fourier plane, and the center of the X-PP (i.e., where the quadrants meet) was aligned with the optic axis until the X-PSFs appeared symmetric on the camera. X-PP alignment was quick, taking only about 15 minutes before each imaging experiment. X-PSFs preserve their pattern when the X-PP is rotated around the optic axis. This property simplifies X-PP alignment and makes the differentiation between X-PSF patterns generated by different probes fairly robust against misalignment.

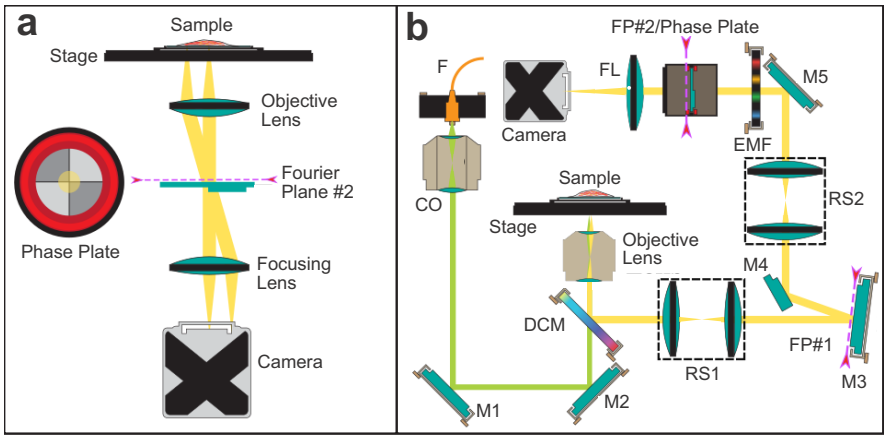

Fig. 2. Optical setup of the microscope. a) A simplified diagram of the detection path of our microscope. The cross-section of the emission beam incident on the phase plate is shown by the bright spot at its center. b) A more detailed diagram of a Vutara 352 super-resolution microscope. Laser light couples to the system via the fiber out-couple F and is collimated by the CO objective. The silver mirrors, M1 and M2 steer the excitation laser light (green) to the sample and M3-M5 mirrors steer the emission light (yellow) to the Orca Fusion BT sCMOS camera. FP#1 and FP#2 are Fourier planes indicated by magenta dashed lines. The Vutara 352 facilitates incorporating a deformable mirror if required at FP#1 and a phase plate at FP#2. The relay lens systems RS1 and RS2 create the FP#1 and FP#2 Fourier planes. EMF is a filter-wheel that can be used to sequentially distinguish fluorophores species. When imaging multiple fluor species simultaneously, the emission light passes through an empty slot in the filter-wheel. The lens FL focuses emission light onto the camera.

2.3. Numerical analysis

We wrote a custom library of classes and scripts in MATLAB to analyze our raw multi-color localization microscopy X-PSF data as described below. Here, we localized the PSFs in three spatial dimensions and sorted them by the fluor type using a maximum likelihood estimation approach by comparing experimental X-PSFs with X-PSFs constructed via a mathematical model.

2.3.1. PSF model

Although many others have modeled the PSF by vector-based diffraction [25,26], scalar diffraction theory was sufficient to describe the X-PSF. We modified the Gibson-Lanni PSF model as described by Kirshner [43], and Born and Wolf [44] with a term representing the phase pattern imparted by

Optics EXPRESS

the X-PP to fit the signal PSFs in our data:

$$U(D) = \exp[ik(n_a - n_p)\ \ \Delta \cdot \Theta(D) + ik\Theta_z(D) + i\psi_{GL}(D)] \tag{1}$$

$$XPSF(x, y, z, k) = \left| \mathcal{A}k \int_0^1 \int_0^{2\pi} U(x, y, z, \rho, \theta)\ \rho\ d\rho\ d\theta \right|^2$$

where ψ_{GL} represents the standard phase terms in the Gibson- Lanni PSF model; Δ is the difference in thickness between the thick and thin regions of the phase plate; n_a and n_p are the indices of refraction for air and the phase plate, respectively; Θ describes the topography of the phase plate, and its maximum value is normalized to unity; and Θ_z describes the optical aberrations incorporated into the X-PSFs from the microscope modeled as weighted Zernike polynomials. The integral is taken over the unit disk, D, which represents the illuminated portion of the Fourier plane. $\mathcal{A}$ is a normalization constant such that the integral of the X-PSF is unity. Finally, (x, y, z) is a point in the image plane of the microscope and k is the wavenumber. The phase plate term is constructed for parallel bundles of rays that are perpendicularly incident on the phase plate. The ray bundles from emitters displaced from the optical axis or focal plane make very small angles with the phase plate, hence the term identifying the phase contribution from the X-PP is still a good approximation for such emitters as well. The X-PSF model is elaborated in the supplemental material.

Fast-Fourier transforms (FFTs) can efficiently calculate a simplification of the diffraction integral representing light propagation of a PSF-engineered microscope [45]. However, we found that padding the numerical representation of the Fourier plane with zeros to increase the FFT sample rate to match the camera's pixel size was too slow for our analysis goals. Instead, we calculated the diffraction integral using a Gaussian cubature formula of the unit disk as given by Cools et al. [46] with the topography of the phase plate being modeled using sigmoid functions.

Accounting for the optical aberrations inherent in our microscope was essential for matching the measured X-PSF and our model X-PSF. We do this by incorporating a weighted sum of Zernike polynomials (Θ_z) – horizontal and vertical tilt, oblique astigmatism, vertical and horizontal coma, and primary spherical aberration – in the diffraction integral (Eq. (1)). We assume that the Zernike aberrations remain the same for all wavelengths and all emitters throughout the sample. Experimentally, we ensure the microscope is properly focused using 150-200 nm diameter fluorescent beads, so we didn't include defocus terms in the Zernike polynomials; furthermore, we employ single-plane imaging, so we left out multi-plane terms from Kirshner et al. [43]. Before imaging biological samples, we extracted the Zernike weights characteristic of the microscope by acquiring multiple X-PSFs from fluorescent beads (FluoSpheres Tetraspeck beads from ThermoFisher) illuminated with 488, 561, and 647 (or 640) nm laser lines (Yellow-Green, Orange, and Dark-Red emission spectra). In this calibration, we acquired a stack of images at different depths (z) within the bead sample and used a maximum likelihood estimation algorithm (see below) to fit the model X-PSF to these experimental X-PSFs. For the fitting, we used a monochromatic representation of the X-PSF corresponding to the peak wavelength of the emission spectra after smoothing the model X-PSF image by Gaussian blurring. Regions of interest (ROI) were selected using a Python blob detection algorithm (Difference of Gaussian method) [47]. The X-PSF intensity distribution is at most 30% broader than the standard Airy PSF for emitters close to the focal plane, which is equivalent to about one camera pixel around the periphery of the PSF; for emitters far away from the focal plane, the breadth of the intensity distribution of the X-PSF is almost the same as for an Airy pattern (see Supplement 1).

2.3.2. Maximum likelihood estimation

With a model of the X-PSF in hand, emitter localization and wavelength estimation are done in two steps. The first step is to guess the emitter wavelength, lateral position on the camera, and

Optics EXPRESS

depth (axial position z) of each experimental X-PSF in the field of view. We make this guess by constructing a lookup table using the Zernike-calibrated X-PSF model. The lookup table has four dimensions: *x, y,* and z spatial coordinates and the spectral coordinate λ. The spatial dimensions of the lookup table consist of the X-PSF model at positions separated by 50 nm in-plane and axially, while the spectral dimension consists of two (or three) monochromatic representations of the calibrated X-PSF.

The initial guess becomes the starting point for the second localization step in which the negative log-likelihood between the data and the model is minimized using a Nelder-Mead simplex algorithm [48]. This second step is done with all four dimensions of the X-PSF (*x, y, z,* and λ). During this part of the analysis, a monochromatic model of the X-PSF is again used because fitting using the Nelder-Mead algorithm with a polychromatic representation of the PSF is too computationally costly. A Gaussian smoothing filter is applied to the Zernike-calibrated monochromatic X-PSFs modeled at the emission peak of each spectrum. We found the Nelder-Mead algorithm to be computationally faster than the Newton-Raphson method because the latter required calculating the Hessian of the objective function. The algorithm records a PSF's spatial and wavelength coordinates after each fit had gone through 3,000 iterations and we bin the localizations considering the fitted wavelengths and then use a hard threshold to determine the associated probe type. The result was passed to the rendering software (Vutara SRX) to produce images with varying statistical filtering criteria. These filters were applied manually by the user to qualitatively optimize the reconstructed super-resolution image.

2.4. Sample preparation and imaging

2.4.1. Fluorescent bead sample preparation

The samples imaged in Fig. 3 were made by diluting ThermoFisher FluoSphere beads (see results for more specific information) in a 1:10^4 ratio from a stock solution in ultra-pure water. A microscope slide was prepared with 15 µl of poly-L-lysine as an adhesive for the beads and was allowed to stand on the slide for ten minutes before the excess was pipetted off. 20 µl of the dilute bead solution was then pipetted onto the slide and dried in a vacuum chamber. Once dry, the area containing the beads was secured with a coverslip using nail polish as a sealer. The sample was mounted on the microscope such that the laser light is incident through the coverslip (#1.5 H). The same sample was used in calibrating the microscope for optical aberrations before biological imaging.

2.4.2. Biological sample preparation

U2OS cells grown in #1.5 H Ibidi chambers (µ-Slide 8 well Cat#80826) at 37°C in 5% CO_2 airgas were fixed in 37°C 3% paraformaldehyde (EMS) and 0.1% glutaraldehyde (EMS) in PEM buffer (100 mM PIPES, 1 mM EGTA, 1 mM $MgCl_2$, pH 7.0) for 15 minutes. Glutaraldehyde autofluorescence was quenched by adding fresh 0.1% sodium borohydride in PBS for 7 minutes. Cells were blocked and permeabilized in blocking buffer (5% donkey serum, 0.1% Saponin (w/v), 0.05% Triton X-100 in PBS) for 45 minutes at room temperature. Cells were incubated within blocking buffer rabbit anti-Tomm20 (abcam AB78547) and mouse anti-HSP60 (R&D systems MAB1800) (Thermo-Fisher) or with mouse anti-alpha tubulin (Sigma) and rabbit anti-detyrosinated tubulin (Sigma). Cells were incubated overnight at 4°C with shaking. Cells were washed 3 to 5 times in PBS. Cells were incubated with secondary antibodies anti- rabbit Alexa Fluor 647 (Thermo-Fisher), anti-mouse CF568 (Biotium), and Phalloidin-Alexa Fluor 488 (Thermo-Fisher) for 1 hour at room temperature. Cells were washed 3 to 5 times in PBS. Cells were postfixed in 4% PFA for 5 minutes at room temperature and washed 3 to 5 times in PBS and cells were imaged in standard Gloxy imaging buffer for dSTORM: 20 mM cysteamine, 1% (v/v) 2-mercaptoethanol, and oxygen scavengers (168 AU glucose oxidase and 1404 AU catalase) in 50 mM Tris, 10 mM NaCl buffer with 10% w/v glucose at pH 8.0.

Optics EXPRESS

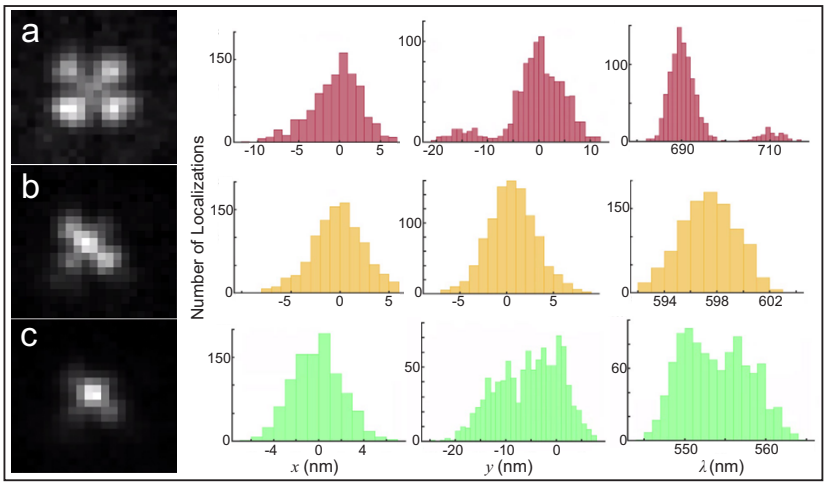

Fig. 3. Simultaneous spatial and spectral localization of three different fluorescent spectra. a) The X-PSF of a TetraSpeck bead illuminated by the 640 nm laser line and its binned localizations for 1,000 camera frames. b) and c) The PSFs of the same bead illuminated by 561 and 488 nm laser lines separately and their corresponding histograms similar to (a).

3. Results

3.1. Ability to distinguish spectra and localization precision

We previously showed in Martineau et al. [49] that the X-PSF geometry is capable of distinguishing between three different species of fluorescent beads (ThermoFisher FluoSpheres: Dark-Red, Orange, and Yellow-Green, prepared as described above) near the focal plane. Here, we quantify the simultaneous spectral and spatial localization capability of the X-PSFs using our localization algorithm for X-PSFs with three different bead colors, as shown in Fig. 3(a) for 1,000 camera frames. We fixed the z coordinate at 50 nm for all localizations, corresponding to the average radius of the beads. The histograms for localizations in x, y, and λ for the three bead spectra are shown in Fig. 3. The X-PSF showed a lateral spatial localization and a spectral localization precision of $\leq$10 nm (FWHM) near the focal plane for Dark-Red (~16,000 photons per PSF and ~50 background photons per pixel) and Orange (~22,000 photons per PSF and ~50 background photons per pixel) PSFs. For Yellow-Green PSFs (~17,000 photons per PSF and ~50 background photons per pixel), the localization precisions were ~15 nm. These photon counts are quite high and the bead diameter is ~100 nm, neither of which are representative of single-molecule localization within biological samples. Nonetheless, this clearly demonstrates the ability of the X-PSF approach to simultaneously obtain high-precision spatial and spectral information.

3.2. Multi-spectral super-resolution imaging of biological samples

We demonstrate simultaneous two-color and three-color dSTORM [50] imaging using the X-PSFs in Vutara 352 microscope. The spectra were localized based only on PSF pattern. We used 10,000 camera frames at 25 ms each to acquire the images. Figure 4(a) shows the x-y plane of a super-resolution image of microtubules composed of α-tubulin tagged with Alexa Fluor 647 (green), and TOMM20 tagged with CF568 on the outer membrane of mitochondria (red) in fixed U2OS cells. The cell sample was illuminated simultaneously by the 640 and 561 nm laser lines. The two protein species are uniquely identifiable. TOMM20 appears interwoven within the microtubule forest as expected. Figure 4(b) shows a portion of the same image along an x-z section. Figure 4(c) shows the single probe images of the segment of Fig. 4(a) that is inside the

Optics EXPRESS

dashed rectangle and Fig. 4(d) shows the wavelength distribution of the localization. For the two-color image, we observed ~3,500 photons per PSF on average over an average background of ~400 photons per pixel.

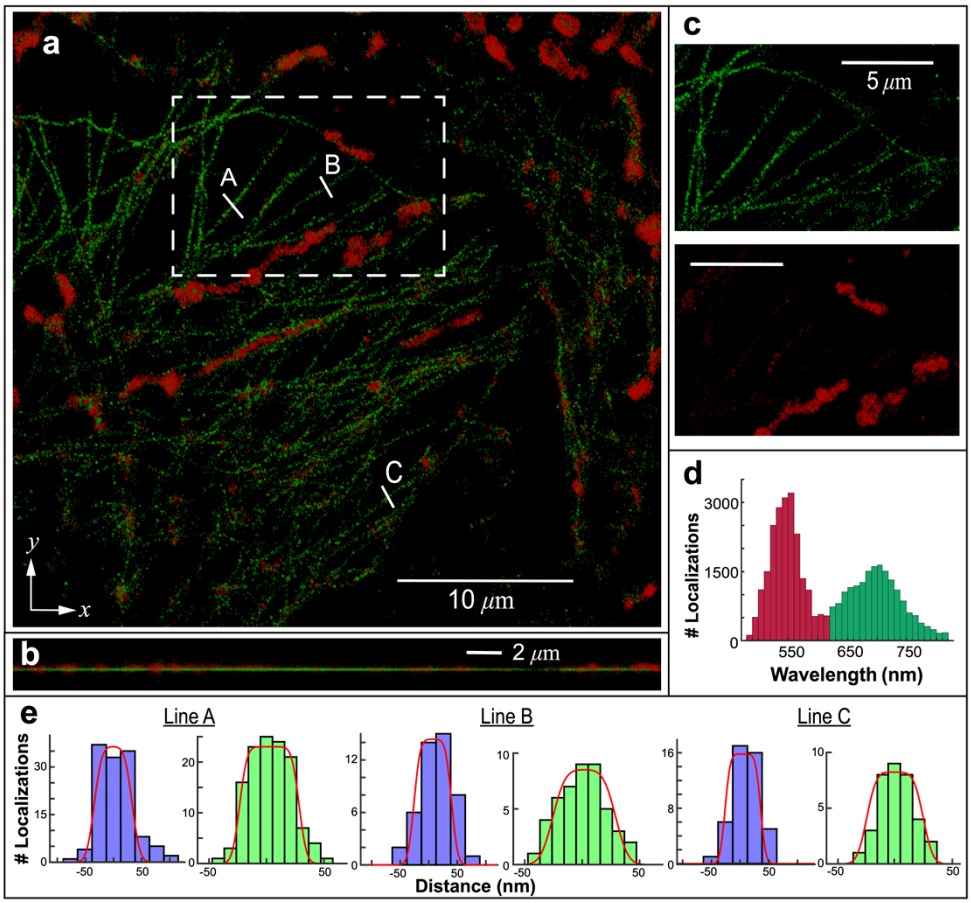

Fig. 4. Two-color fixed cell imaging. a) Tubulin, labeled with Alexa Fluor 647, is in green; TOMM20, labeled with CF568, is in red. The sample was illuminated simultaneously by 640 and 561 nm laser lines, and the emission wavelength was identified based only on PSF shape without emission filters. The excitation intensity for the two laser lines was ~5 kW/cm^2. A 405 nm laser at ~1 W/cm^2 was used to control fluorophore blinking. b) An edge-on view (x-z cross section) of the data in (a) from $y = 0$ to the lower edge of the dashed box. c) Single probe/color renditions of the rectangular segment indicated by the dashed box in (a). d) The wavelength distribution of localizations color-coded according to how they were rendered; the red-green threshold value was $\lambda = 620$ nm. e) The density of localizations along the three line-segments labeled A-C in (a). Blue/green histograms indicate the density of localizations across the width (x-y plane) and depth (z) of a microtubule, respectively. The convolution of a Gaussian and a rectangular function were fit to each histogram as shown in red. For the width (blue) histograms, the Gaussian FWHM were 25, 20 and 16 nm (A-C) and the width of the rectangular function was 68, 66 and 61 nm. For the depth (green) histograms, the Gaussian FWHM were 12, 20 and 15 nm A-C and the width of the rectangular function was 52, 55, and 50 nm.

Microtubules provide an excellent reference to test the localization precision because of their extended linear nature and their known width. Native microtubules are 25 nm in diameter [51],

Optics EXPRESS

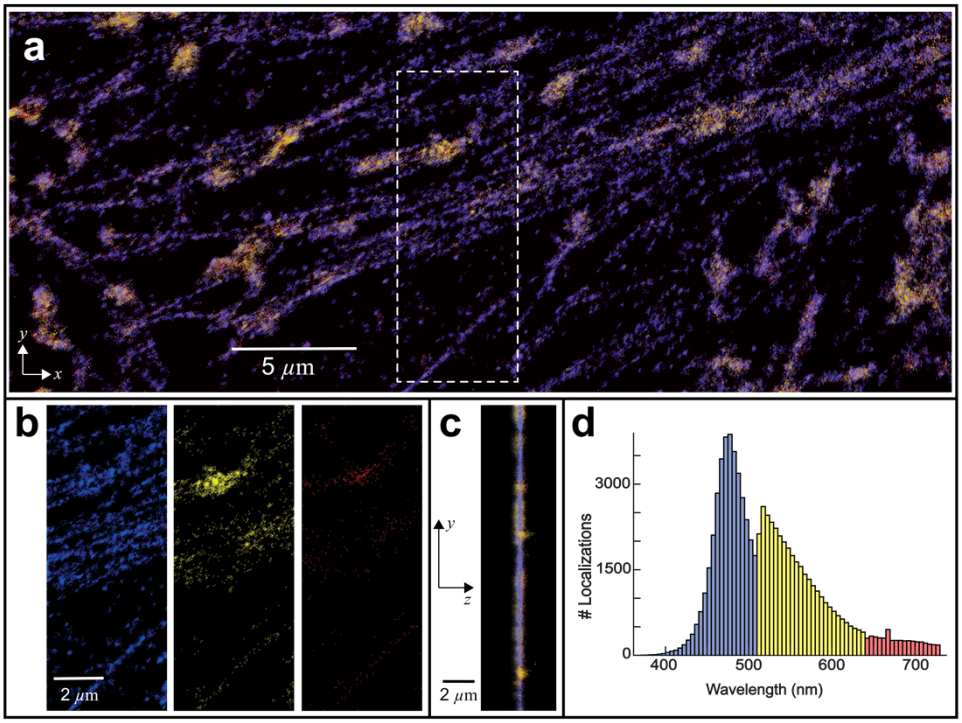

Fig. 5. Three-color fixed cell imaging. a) Tubulin, labeled with Alexa Fluor 488, is rendered in blue; TOMM20, labeled with CF568, is rendered in yellow; ds-DNA, labeled with Alexa Fluor 647 is rendered in red. The cell sample was illuminated simultaneously by the 488, 561 and 640 nm laser lines, and the spectra were localized based only on PSF pattern without using emission filters. The excitation intensity for the three laser lines was ~3 kW/cm^2. A 405 nm laser was used at ~1 W/cm^2 to control the fluorophore blinking. b) Single probe image renditions of the area indicated by the dashed rectangle in (a). c) An edge-on view (y-z cross section) of the data in (a) from $x = 0$ to the left edge of the dashed box. d) The wavelength distribution of localizations color-coded according to how they were rendered; the threshold values separating the probes are 510 and 640 nm.

and antibody-coated microtubules have been measured at 60-nm diameter by electron microscopy [52]. The histograms in Fig. 4(e) show the density of localizations across three microtubule strands labeled A, B, and C in Fig. 4(a). We fitted a convolution of a Gaussian and a rectangular function (indicating the finite width of an antibody-stained microtubule) to each histogram. To estimate our localization precision, we use the FWHM of the Gaussians [13,24]. The FWHM of these Gaussian fits are 16 - 25 nm in the x-y plane and 12 - 20 nm in the z direction across a microtubule. The calculated width of an antibody-stained microtubule is 65 nm on average in the x-y plane and 52 nm in z, which suggests that there may be a small systematic underestimation of lengths along the axial direction. In any case, proper calibration of the imaging system, which takes into account various aberrations via Zernike coefficients in the model PSF, is critical to obtain high localization precision, particularly in the axial direction.

We note that the CF568 label density in Fig. 4 is quite high, giving the impression of saturation in the red channel for some regions of the image. However, each emitter was rendered as a distinct point, with those in the focal plane having the highest opacity. Based on the lateral size of the fitted X-PSFs, the biological cell is thicker in the lower half of the image, which makes it more likely for microtubules to adopt out-of-plane orientations, and also allows for a higher density of

Optics EXPRESS

microtubules in this region. These factors can lead to more occurrences of overlapping green X-PSFs, which are rejected by our fitting algorithm, and also less contiguous microtubule images since they have a larger chance of being oriented vertically. The lateral localization precision in the thicker regions of the cell can also be degraded somewhat since emitters above and below the focal plane have more diffuse PSFs.

Figure 5(a) shows the *x*-*y* plane of a three-color super-resolution image of α-tubulin tagged with Alexa Fluor 488 (blue), TOMM20 tagged with CF568 (yellow), and ds-DNA inside mitochondria tagged with Alexa Fluor 647 (red) in fixed U2OS cells. The cell sample was illuminated simultaneously by 488, 561 and 640 nm laser lines. The ds-DNA localizations are contained inside mitochondria as expected. We observed ∼1, 200 photons per PSF on average for the localizations in the green channel and ∼ 2,500 for the other two channels at a background of ∼130 photons per pixel. There is considerable cross talk between the green and the orange channels (rendered in blue and yellow, respectively) when compared to the orange and red channels.

4. Discussion

The goal in SMLM is to localize multiple emitters at a spatial scale meaningful to a protein – specifically at the diameter of a typical protein, ∼10 nm. Here, we observe that X-PSFs created by a four-quadrant glass phase plate can be used for multi-spectral imaging with localization precision comparable to other PSF families. The discussion below evaluates the localization precision of the X-PSF, its ability to distinguish spectra, and its utility for imaging multiple probes under simultaneous excitation and detection.

4.1. Localization precision

We use the Cramér-Rao lower bound (CRLB), referred to as σ^2_{min} (statistical variance) in this paper, to estimate the best-case precision of the X-PSF in the *x, y, z*, and λ dimensions. We represent the center coordinates of a PSF at the image plane of the microscope as x_0 and y_0, the axial coordinate relative to the focal plane of the microscope (i.e., at the sample) as z_p, and a representative wavelength for the emission spectra as λ. As others have noted [53–55], CRLB is calculated by inverting the Fisher information matrix and taking its diagonal elements as the *minimum* possible variance $\sigma^2_{min} = [\sigma^2_{min,x_0}, \sigma^2_{min,y_0}, \sigma^2_{min,z_p}, \sigma^2_{min,\lambda}]$ around the actual value that can be achieved when measuring the unknowns *x, y, z*, and λ. Assuming shot noise only, the Fisher information matrix $\mathrm{I_k}$ is given by Eq. (2) where $\mu_k(\vec{\theta})$ is the theoretical (model) X-PSF given by Eq. (1), and $\vec{\theta} = (\mathrm{x_0}, \mathrm{y_0}, \mathrm{z_p}, \lambda)$ are the parameters being estimated:

$$I_k(\vec{\theta}) = \left[\frac{1}{\mu_k}\frac{\partial \mu_k}{\partial \theta_i}\frac{\partial \mu_k}{\partial \theta_j}\right]. \tag{2}$$

The theoretical precision in $\vec{\theta}$ for the X-PSFs calculated as the $\sigma^2_{min} \equiv$ CRLB at three different emission wavelengths ($\lambda = 680$, 585, and 515 nm) is shown in Fig. 6(a)-(c) respectively. For this calculation, we neglected Zernike aberrations and assumed that light detection follows Poissonian statistics and that the background is uniform across all pixels. We observed 1,000-5,000 photons per PSF for the cells, and therefore the precisions are plotted at 2,500 photons as an average. Figure 6 suggests that the axial localization precision is expected to be worst at the focal plane, since the X-PSFs are symmetric at the focal plane and the asymmetry that allows to distinguish between the negative and the positive axial values is small at the vicinity of the focal plane. Since the X-PSF is asymmetric far away from the focal plane, the axial localizability improves (see Supplement 1).

Optics EXPRESS

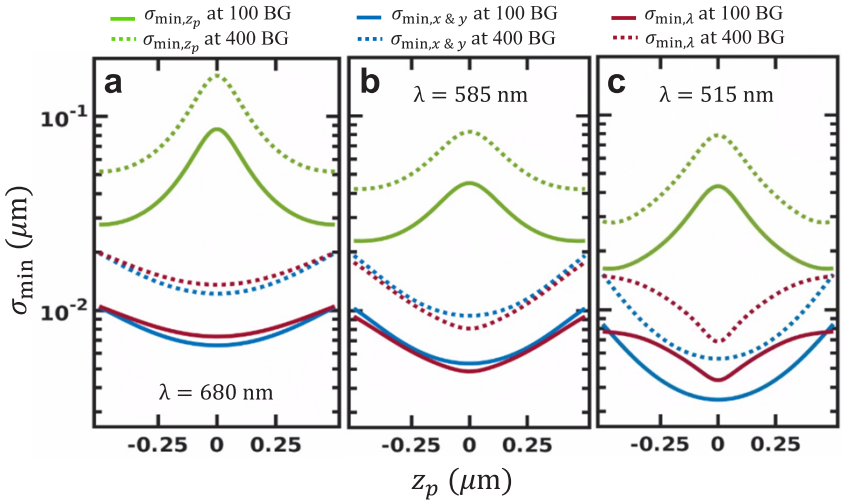

Fig. 6. Theoretical precision of the X-PSF as a function of position relative to the focal plane, z_p, at different wavelengths for 2,500 photons per PSF at 100 and 400 background photons per pixel. The wavelengths are 680 nm (a), 585 nm (b), and 515 nm (c). The green, blue, and red curves correspond to axial direction, the in-plane directions, and the wavelength respectively. Solid lines correspond to 100 background photons per pixel and the dotted lines to 400. The wavelengths roughly correspond to the peak wavelengths for the "Dark-Red", "Orange", and "Yellow-Green" FluoSpheres spectra in Fig. 3.

4.2. *Simultaneous multicolor imaging*

During simultaneous multicolor imaging the background signal can be elevated due to overlapping PSFs from the different fluor species, from the same species, or cell autofluorescence. Any of these background sources, which are more prominent in simultaneous multicolor imaging relative to single-color imaging, obscure the structure of the X-PSF and it is somewhat more difficult to identify individual emitters by their spectra. Thus, a fluorophore species with significantly weaker emission compared to others in the vicinity may get lost in the background, and it may be difficult for the fitting algorithm to identify the regions of interest and also to converge on a solution. For instance, Alexa Fluor 488 PSFs in our data acquisitions yielded only half the photons as the other two fluors. This may have contributed to the cross-talk between green and orange channels. Theoretically, limiting blinking rates and editing out poor wavelength localizations could limit such miscalls but would also reduce localization density.

Another challenge in simultaneous multicolor imaging is controlling the independent blinking rates of each fluor species. To restore fluors to the ground state, we use a 405 nm laser which illuminates all fluors simultaneously. But the photophysics of each fluor species and the label density for each probe may require a different 405 nm laser intensity to optimize blinking. In addition, highly concentrated clusters of a protein and unstable triplet states can lead to regions that require a different 405 nm laser intensity to ensure that PSFs are sufficiently sparse to be localized. Matching PSF densities from different fluors might require diluting the fluorescent labels of particular proteins.

4.3. *Differentiating between probe species using the X-PSF*

The ability of the X-PSF to differentiate between fluor species based on their emission spectra was studied using sequential imaging of a U2OS cell and Monte-Carlo simulations using experimental parameters. In Fig. 7 we show simulations of correct spectral assignments for the X-PSF as

Optics EXPRESS

a function of the number of background photons per pixel for the three dyes Alexa Fluor 647 (tagging microtubules), CF 568 (tagging mitochondria), and Alexa Fluor 488 (tagging clathrin), and the rendered image of the sequential imaging (control experiment) to compare with the simulations. The simulated sample background is primarily caused by autofluorescence and fluorescence from out-of-focus emitters, both belonging to the same or to different probe species. We simulated noisy X-PSFs by incorporating the sample background, shot noise in photon detection, and camera readout noise to the model X-PSFs at multiple spatial coordinates for a specific probe. Furthermore, we employed the same localization algorithm used for biological data analysis (Figs. 4 and 5) to determine the probe type. We used a distribution of photons similar to the photon distribution observed in the control experiment and that of with an average of ~ 3,500 photons per PSF. The number of correct identifications is the number of X-PSFs correctly sorted by the algorithm as a percentage of the total number of the input X-PSFs belonging to that probe as a function of the number of background photons. For a simulated background of 100 photons per pixel, correct identifications for Alexa Fluor 647, CF568, and Alexa Fluor 488 probes were 95%, 89%, and 94%, respectively.

We prepared fixed U2OS cells with the same three distinct fluorophore labels to reproduce the imaging conditions of biological samples; however, the labeling efficiency of this fixed sample was not sufficient to yield high-quality three-color images. We imaged this sample sequentially (not simultaneously) with three laser lines and identified the fluorophore species using emission filters. We then applied our X-PSF analysis algorithm to the same sequential data set, and extracted the fluorophore species from the shape of each PSF. For a background of ~100 photons per pixel, identifications were correctly reported for 95%, 80%, and 89% of the localizations for Alexa Fluor 647, CF 568, and Alexa Fluor 488, respectively. Truth tables for the simulations and the control experiment can be found in Supplement 1. Mismatches between the simulation and the actual data could be due to several factors. For example, it is difficult to precisely know the number of photons per PSF in the experimental data as has been reported elsewhere [56]. In addition, variations in the background over the region of interest and having multiple (overlapping) PSFs in the same region of interest, both of which become more prominent with simultaneous multicolor imaging, increase the probability of mismatches compared to single-color or sequential multicolor imaging.

Using an algorithmic approach to localize engineered PSFs can be simpler and easier to implement when compared to deep learning methods. Unlike a LCSLM, our phase mask is a transmissive, polarization insensitive, and an inexpensive glass optic that can be easily inserted into a commercial microscope, as was done here. The X-PSF models are evaluated at only 88 points (Gaussian Cubature model) which is computationally inexpensive. The PSF shapes are mathematically calculated for each x, y, z coordinate combination with the prior knowledge of the emission spectra, which eliminates the need of acquiring training data for every new set of conditions. It is important to note that properly calibrating the PSF model to closely resemble the data is critical and can be somewhat challenging.

The Gibson-Lanni model is derived by considering emitters at arbitrary positions within a sample. However, the phase plate term and the Zernike aberration terms impose limitations on the maximum depth that the model can be applied. As explained in the Supplement 1, the collected light is approximated as parallel bundles of rays that are parallel to the optic axis (i.e., perpendicular to the surface of the phase plate). Ray bundles for emitters near the lateral edges of the field of view acquire a small angle relative to the optic axis, which is less than 10° for a 40-μm field of view. Axially, emitters more than ±500 nm from the focal plane are not able to be resolved, due to crosstalk between the axial position and spectral fitting parameters, and because emitters above and below the focal plane yield ray bundles that are diverging or converging somewhat. We assume in the calibrations that the Zernike aberration weights are the same for all wavelengths at all spatial locations, which may not be true and could produce deviations from the

Optics EXPRESS

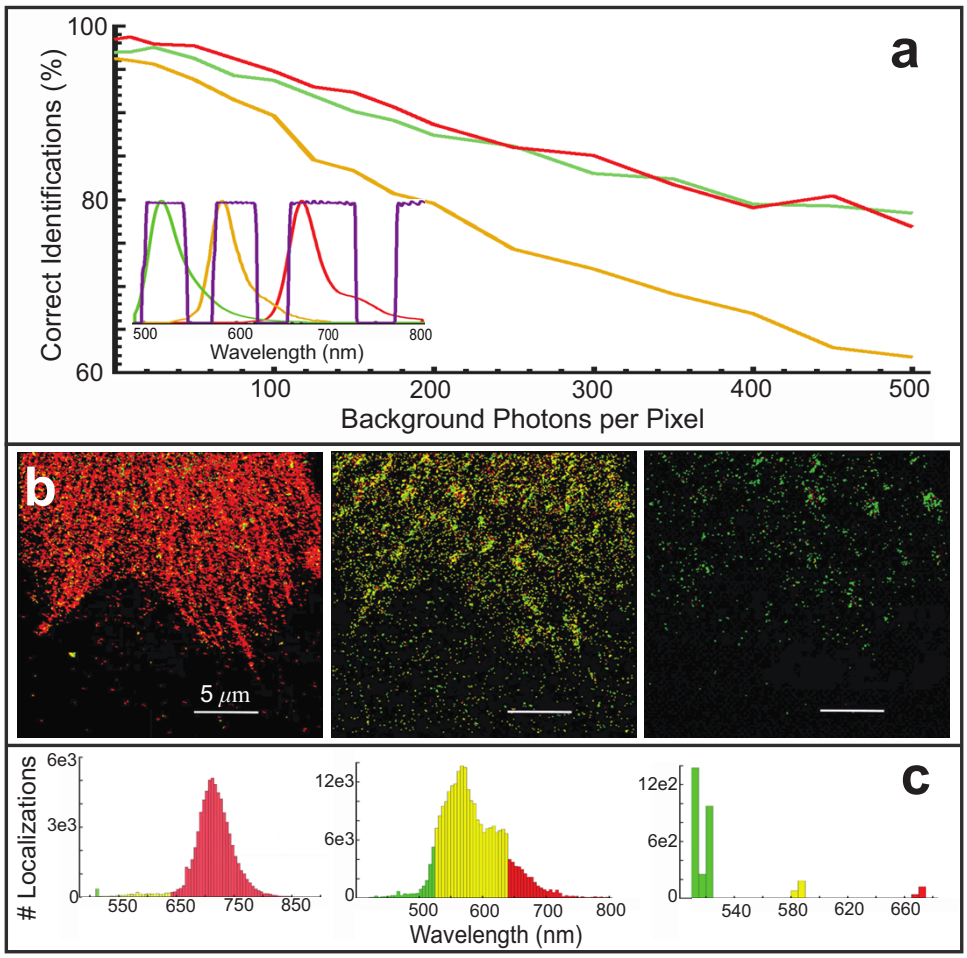

Fig. 7. Spectral distinguishability of the X-PSFs using a Monte-Carlo simulation. a) The simulated percentage of correct spectral identifications for the probes AXF 647 (red), CF 568 (orange), and AXF 488 (green) are plotted as a function of the number of background photons per camera pixel. In the simulations, we used a distribution of photons similar to the photon distribution observed in the control experiment and the biological imaging in Fig. 4 having an average of ~3,500 photons per PSF. The three spectra are shown in the inset with the transmission windows of the dichroic filter denoted by the purple lines. b) The *x*-*y* plane of the identifications for red, orange and green channels from left to right of the control experiment (sequential imaging of each probe and separation using emission filters). The identifications are rendered in red, yellow, and green respectively. c)The histograms corresponding to the localizations in (b) are top to bottom. The threshold values of 525 nm and 640 nm are common to all the channels and were chosen qualitatively after observing the histograms.

Optics EXPRESS

X-PSF models when the focal plane is positioned deep into a sample. We have used the X-PP to image only regions in a sample that are 1-2 μm thick. In our experience the calibration is mostly affected by the placement of the phase plate at the center of the beam. If it is not centered, we would need to introduce additional fitting parameters for the lateral phase plate offsets.

5. Conclusion and future work

A four-quadrant glass phase plate can adequately alter the structure of PSFs to differentiate three fluorescent emitters for localization microscopy. We use the scalar Gibson-Lanni model with Gaussian cubature representation of the phase plate topography and the log-likelihood estimation to localize the emitters simultaneously in x, y, z, and λ. Overall, our approach is adaptable to various microscopy methods and the implementation is straightforward. The X-PSF, which results from placing the phase plate in the Fourier plane of the detection arm of a microscope, allows single molecules to be localized with a precision of 21 nm laterally and 17 nm axially. The proof-of-principle measurements using dye-doped beads suggests that with sufficient signal, it could be possible to resolve 10 nm spectral differences at the focal plane using our X-PSF approach. We have demonstrated simultaneous imaging of two-color and three-color fixed U2OS cells with the X-PSF. The X-PSF may improve the capabilities of new super-resolution imaging techniques such as spectral multiplexing, and biplane imaging [39,40]. The utility of X-PSFs for simultaneous live-cell imaging may be improved further by using quantum dots that have narrow emission spectra and a large fluorescent yield [57,58]. The goal is to identify spectra at nanometer-scale spatial resolution at millisecond-scale temporal resolution, for long timespans of cellular evolution.

This work also highlights some inherent challenges associated with simultaneous multicolor imaging. In particular, the rate of overlapping PSFs increases when multiple fluor species are imaged simultaneously onto the detector; this causes an increase in the background signal for any particular PSF, and also leads to non-uniform background fields, both of which compromise the spatial and spectral localizability. In the future, we will study how these challenges could be addressed, for example, by cycling quickly between different illumination lasers and synchronized readout of corresponding camera frames or using dyes with comparable emission intensities and complementing blinking rates. While this will slow down image acquisition relative to simultaneous imaging, it should yield more precise localizations, which may be the more important factor for some experiments.

One goal for future work is to improve the model PSFs to better account for aberrations and spectral factors, making our approach more robust and precise. For this work, we qualitatively chose the thickness of the four-quadrant phase plate such that the red and green X-PSFs show canonical forms. We intend to introduce an optimization scheme for the thickness to yield X-PSFs that are more efficient for different systems such as the properties of the set of fluorescent tags, level of background, and the required imaging depth. The eventual goal is to localize multiple proteins in three dimensions in a living cell.

Funding. National Science Foundation (2014862); National Institute of Neurological Disorders and Stroke (NS034307); Department of Physics and Astronomy, University of Utah; Erik M. Jorgensen is an investigator of the Howard Hughes Medical Institute.

Acknowledgments. The authors acknowledge Drs. Carl Ebeling and Wayne Davis for their insight and feedback, and The University of Utah nanofabrication facility where the phase plate was fabricated.

Disclosures. The authors declare no conflicts of interest.

Data Availability. Data underlying the results presented in this paper are not publicly available at this time but may be obtained from the authors upon reasonable request.

Supplemental document. See Supplement 1 for supporting content.

Optics EXPRESS

References

1. M. Lelek, M. T. Gyparaki, G. Beliu, F. Schueder, J. Griffié, S. Manley, R. Jungmann, M. Sauer, M. Lakadamyali, and C. Zimmer, "Single-molecule localization microscopy," Nat. Rev. Methods Primers **1**(1), 39 (2021).
2. L. Möckl and W. E. Moerner, "Super-resolution Microscopy with Single Molecules in Biology and Beyond–Essentials, Current Trends, and Future Challenges," J. Am. Chem. Soc. **142**(42), 17828–17844 (2020).
3. E. Betzig, G. H. Patterson, R. Sougrat, O. W. Lindwasser, S. Olenych, J. S. Bonifacino, M. W. Davidson, J. Lippincott-Schwartz, and H. F. Hess, "Imaging Intracellular Fluorescent Proteins at Nanometer Resolution," Science **313**(5793), 1642–1645 (2006).
4. G. Shtengel, J. A. Galbraith, C. G. Galbraith, J. Lippincott-Schwartz, J. M. Gillette, S. Manley, R. Sougrat, C. M. Waterman, P. Kanchanawong, M. W. Davidson, R. D. Fetter, and H. F. Hess, "Interferometric fluorescent super-resolution microscopy resolves 3D cellular ultrastructure," Proc. Natl. Acad. Sci. U.S.A. **106**(9), 3125–3130 (2009).
5. M. F. Juette, T. J. Gould, M. D. Lessard, M. J. Mlodzianoski, B. S. Nagpure, B. T. Bennett, S. T. Hess, and J. Bewersdorf, "Three-dimensional sub–100 nm resolution fluorescence microscopy of thick samples," Nat. Methods **5**(6), 527–529 (2008).
6. S. T. Hess, T. P. K. Girirajan, and M. D. Mason, "Ultra-High Resolution Imaging by Fluorescence Photoactivation Localization Microscopy," Biophys. J. **91**(11), 4258–4272 (2006).
7. E. A. Mukamel, H. Babcock, and X. Zhuang, "Statistical Deconvolution for Superresolution Fluorescence Microscopy," Biophys. J. **102**(10), 2391–2400 (2012).
8. M. J. Rust, M. Bates, and X. Zhuang, "Sub-diffraction-limit imaging by stochastic optical reconstruction microscopy (STORM)," Nat Methods **3**(10), 793–796 (2006).
9. B. Huang, W. Wang, M. Bates, and X. Zhuang, "Three-Dimensional Super-Resolution Imaging by Stochastic Optical Reconstruction Microscopy," Science **319**(5864), 810–813 (2008).
10. A. Sharonov and R. M. Hochstrasser, "Wide-field subdiffraction imaging by accumulated binding of diffusing probes," Proc. Natl. Acad. Sci. U.S.A. **103**(50), 18911–18916 (2006).
11. J. Schnitzbauer, M. T. Strauss, T. Schlichthaerle, F. Schueder, and R. Jungmann, "Super-resolution microscopy with DNA-PAINT," Nat Protoc **12**(6), 1198–1228 (2017).
12. Y. M. Sigal, R. Zhou, and X. Zhuang, "Visualizing and discovering cellular structures with super-resolution microscopy," Science **361**(6405), 880–887 (2018).
13. M. Bates, B. Huang, G. T. Dempsey, and X. Zhuang, "Multicolor Super-Resolution Imaging with Photo-Switchable Fluorescent Probes," Science **317**(5845), 1749–1753 (2007).
14. M. S. Gunewardene, F. V. Subach, T. J. Gould, G. P. Penoncello, M. V. Gudheti, V. V. Verkhusha, and S. T. Hess, "Superresolution Imaging of Multiple Fluorescent Proteins with Highly Overlapping Emission Spectra in Living Cells," Biophys. J. **101**(6), 1522–1528 (2011).
15. L. J. Friedman, J. Chung, and J. Gelles, "Viewing Dynamic Assembly of Molecular Complexes by Multi-Wavelength Single-Molecule Fluorescence," Biophys. J. **91**(3), 1023–1031 (2006).
16. I. Testa, C. A. Wurm, R. Medda, E. Rothermel, C. von Middendorf, J. Fölling, S. Jakobs, A. Schönle, S. W. Hell, and C. Eggeling, "Multicolor Fluorescence Nanoscopy in Fixed and Living Cells by Exciting Conventional Fluorophores with a Single Wavelength," Biophys. J. **99**(8), 2686–2694 (2010).
17. S. Jia, J. C. Vaughan, and X. Zhuang, "Isotropic three-dimensional super-resolution imaging with a self-bending point spread function," Nat. Photonics **8**(4), 302–306 (2014).
18. Y. Shechtman, L. E. Weiss, A. S. Backer, S. J. Sahl, and W. E. Moerner, "Precise Three-Dimensional Scan-Free Multiple-Particle Tracking over Large Axial Ranges with Tetrapod Point Spread Functions," Nano Lett. **15**(6), 4194–4199 (2015).
19. I. Izeddin, M. El Beheiry, J. Andilla, D. Ciepielewski, X. Darzacq, and M. Dahan, "PSF shaping using adaptive optics for three-dimensional single-molecule super-resolution imaging and tracking," Opt. Express **20**(5), 4957 (2012).
20. O. Zhang and M. D. Lew, "Single-molecule orientation localization microscopy II: a performance comparison," J. Opt. Soc. Am. A **38**(2), 288 (2021).
21. G. Grover, K. DeLuca, S. Quirin, J. DeLuca, and R. Piestun, "Super-resolution photon-efficient imaging by nanometric double-helix point spread function localization of emitters (SPINDLE)," Opt. Express **20**(24), 26681 (2012).
22. D. Baddeley, M. B. Cannell, and C. Soeller, "Three-dimensional sub-100 nm super-resolution imaging of biological samples using a phase ramp in the objective pupil," Nano Res. **4**(6), 589–598 (2011).
23. M. N. Bongiovanni, J. Godet, M. H. Horrocks, L. Tosatto, A. R. Carr, D. C. Wirthensohn, R. T. Ranasinghe, J.-E. Lee, A. Ponjavic, J. V. Fritz, C. M. Dobson, D. Klenerman, and S. F. Lee, "Multi-dimensional super-resolution imaging enables surface hydrophobicity mapping," Nat. Commun. **7**(1), 13544 (2016).
24. Y. Shechtman, L. E. Weiss, A. S. Backer, M. Y. Lee, and W. E. Moerner, "Multicolour localization microscopy by point-spread-function engineering," Nat. Photonics **10**(9), 590–594 (2016).
25. C. Smith, M. Huisman, M. Siemons, D. Grünwald, and S. Stallinga, "Simultaneous measurement of emission color and 3D position of single molecules," Opt. Express **24**(5), 4996 (2016).
26. J. Broeken, B. Rieger, and S. Stallinga, "Simultaneous measurement of position and color of single fluorescent emitters using diffractive optics," Opt. Lett. **39**(11), 3352 (2014).

Optics EXPRESS

27. T. Huang, C. Phelps, J. Wang, L.-J. Lin, A. Bittel, Z. Scott, S. Jacques, S. L. Gibbs, J. W. Gray, and X. Nan, "Simultaneous Multicolor Single-Molecule Tracking with Single-Laser Excitation via Spectral Imaging," Biophys. J. **114**(2), 301–310 (2018).
28. Z. Wang, Y. Cai, Y. Liang, X. Zhou, S. Yan, D. Dan, P. R. Bianco, M. Lei, and B. Yao, "Single shot, three-dimensional fluorescence microscopy with a spatially rotating point spread function," Biomed. Opt. Express **8**(12), 5493–5506 (2017).
29. Y. Zhou and G. Carles, "Precise 3D particle localization over large axial ranges using secondary astigmatism," Opt. Lett. **45**(8), 2466 (2020).
30. Y. Zhou, P. Zammit, V. Zickus, J. M. Taylor, and A. R. Harvey, "Twin-Airy Point-Spread Function for Extended-Volume Particle Localization," Phys. Rev. Lett. **124**(19), 198104 (2020).
31. A. Meiri, C. G. Ebeling, J. Martineau, Z. Zalevsky, J. M. Gerton, and R. Menon, "Interference based localization of single emitters," Opt. Express **25**(15), 17174 (2017).
32. Y.-L. Wu, P. Hoess, A. Tschanz, U. Matti, M. Mund, and J. Ries, "Maximum-likelihood model fitting for quantitative analysis of SMLM data," Nat. Methods **20**(1), 139–148 (2023).
33. E. Nehme, D. Freedman, R. Gordon, B. Ferdman, L. E. Weiss, O. Alalouf, T. Naor, R. Orange, T. Michaeli, and Y. Shechtman, "DeepSTORM3D: dense 3D localization microscopy and PSF design by deep learning," Nat. Methods **17**(7), 734–740 (2020).
34. A. Speiser, L.-R. Müller, P. Hoess, U. Matti, C. J. Obara, W. R. Legant, A. Kreshuk, J. H. Macke, J. Ries, and S. C. Turaga, "Deep learning enables fast and dense single-molecule localization with high accuracy," Nat. Methods **18**(9), 1082–1090 (2021).
35. Y. Hyun and D. Kim, "Development of Deep-Learning-Based Single-Molecule Localization Image Analysis," Int. J. Mol. Sci. **23**(13), 6896 (2022).
36. P. Zelger, K. Kaser, B. Rossboth, L. Velas, G. J. Schütz, and A. Jesacher, "Three-dimensional localization microscopy using deep learning," Opt. Express **26**(25), 33166 (2018).
37. E. Hershko, L. E. Weiss, T. Michaeli, and Y. Shechtman, "Multicolor localization microscopy and point-spread-function engineering by deep learning," Opt. Express **27**(5), 6158 (2019).
38. S. Fernando, J. Martineau, E. Jorgensen, and J. Gerton, "Optimizing Point Spread Functions to Discern Highly Overlapping Emission Spectra," Microsc. Microanal. **27**(S1), 864–867 (2021).
39. C. M. Winterflood, E. Platonova, D. Albrecht, and H. Ewers, "Dual-Color 3D Superresolution Microscopy by Combined Spectral-Demixing and Biplane Imaging," Biophys. J. **109**(1), 3–6 (2015).
40. N. Opatovski, Y. Shalev Ezra, L. E. Weiss, B. Ferdman, R. Orange-Kedem, and Y. Shechtman, "Multiplexed PSF Engineering for Three-Dimensional Multicolor Particle Tracking," Nano Lett. **21**(13), 5888–5895 (2021).
41. D. Malacara, "Optical Shop Testing D. Malacara, Twyman–Green Interferometer (John Wiley Sons, Ltd, 2007), chap. 2, pp. 46–96," in *Optical Shop Testing*, 3rd ed. (John Wiley & Sons, 2007), pp. 46–96.
42. D. Malacara, "H. Schreiber and J. H. Bruning, Phase Shifting Interferometry (John Wiley Sons, Ltd, 2007), chap. 14, pp. 547–666," in *Optical Shop Testing*, 3rd ed. (John Wiley & Sons, 2007), pp. 547–666.
43. H. Kirshner, F. Aguet, D. Sage, and M. Unser, "3-D PSF fitting for fluorescence microscopy: implementation and localization application: 3-D PSF FITTING FOR FLUORESCENCE MICROSCOPY," J. Microsc. **249**(1), 13–25 (2013).
44. M. Born and E. Wolf, *Principles of Optics: Electromagnetic Theory of Propagation, Interference and Diffraction of Light*, 6th ed (Pergamon Press, 1980).
45. M. A. Thompson, J. M. Casolari, M. Badieirostami, P. O. Brown, and W. E. Moerner, "Three-dimensional tracking of single mRNA particles in Saccharomyces cerevisiae using a double-helix point spread function," Proc. Natl. Acad. Sci. U. S. A. **107**(42), 17864–17871 (2010).
46. R. Cools and K. J. Kim, "A survey of known and new cubature formulas for the unit disk," Korean J. Comput. & Appl. Math. **7**(3), 477–485 (2000).
47. S. Van Der Walt, J. L. Schönberger, J. Nunez-Iglesias, F. Boulogne, J. D. Warner, N. Yager, E. Gouillart, and T. Yu, "scikit-image: image processing in Python," PeerJ **2**, e453 (2014).
48. J. C. Lagarias, J. A. Reeds, M. H. Wright, and P. E. Wright, "Convergence Properties of the Nelder–Mead Simplex Method in Low Dimensions," SIAM J. Optim. **9**(1), 112–147 (1998).
49. J. T. Martineau, E. M. Jorgensen, R. Menon, and J. Gerton, "Precisely Localizing Wavelength Sensitive Point-Spread Functions Engineered With a Silicon Oxide Phase Plate," Microsc. Microanal. **24**(S1), 1364–1365 (2018).
50. J. Xu, H. Ma, and Y. Liu, "Stochastic Optical Reconstruction Microscopy (STORM)," Curr. Protoc. Cytom. 81(1), (2017).
51. C. Bouchet-Marquis, B. Zuber, A.-M. Glynn, M. Eltsov, M. Grabenbauer, K. N. Goldie, D. Thomas, A. S. Frangakis, J. Dubochet, and D. Chrétien, "Visualization of cell microtubules in their native state," Biol. Cell **99**(1), 45–53 (2007).
52. K. Weber, P. C. Rathke, and M. Osborn, "Cytoplasmic microtubular images in glutaraldehyde-fixed tissue culture cells by electron microscopy and by immunofluorescence microscopy," Proc. Natl. Acad. Sci. U.S.A. **75**(4), 1820–1824 (1978).
53. J. Chao, S. Ram, T. Lee, E. S. Ward, and R. J. Ober, "Investigation of the numerics of point spread function integration in single molecule localization," Opt. Express **23**(13), 16866 (2015).

Optics EXPRESS

54. A. S. Backer and W. E. Moerner, "Extending Single-Molecule Microscopy Using Optical Fourier Processing," J. Phys. Chem. B **118**(28), 8313–8329 (2014).
55. R. J. Ober, S. Ram, and E. S. Ward, "Localization Accuracy in Single-Molecule Microscopy," Biophys. J. **86**(2), 1185–1200 (2004).
56. Y. Shechtman, S. J. Sahl, A. S. Backer, and W. E. Moerner, "Optimal Point Spread Function Design for 3D Imaging," Phys. Rev. Lett. **113**(13), 133902 (2014).
57. J. K. Jaiswal and S. M. Simon, "Potentials and pitfalls of fluorescent quantum dots for biological imaging," Trends Cell Biol. **14**(9), 497–504 (2004).
58. H. M. Gil, T. W. Price, K. Chelani, J.-S. G. Bouillard, S. D. J. Calaminus, and G. J. Stasiuk, "NIR-quantum dots in biomedical imaging and their future," iScience **24**(3), 102189 (2021).

Supplemental Document

Optics EXPRESS

Simultaneous spectral differentiation of multiple fluorophores in super-resolution imaging using a glass phase plate: supplement

SANDUNI I. FERNANDO,[1] JASON T. MARTINEAU,[1] ROBERT J. HOBSON,[2] THIEN N. VU,[2] BRIAN BAKER,[3] BRIAN D. MUELLER,[2] RAJESH MENON,[4] ERIK M. JORGENSEN,[2] AND JORDAN M. GERTON[1,*]

[1] *University of Utah Department of Physics and Astronomy, 201 James Fletcher Bldg. 115 S. 1400 E Salt Lake City, UT 84112-0830, USA*
[2] *University of Utah School of Biological Sciences, 257 South 1400 East Salt Lake City, Utah 84112, USA*
[3] *University of Utah Nanofab 36 S. Wasatch Drive, SMBB Room 2500 Salt Lake City, UT 84112, USA*
[4] *University of Utah Department of Electrical and Computer Engineering 50 S. Central Campus Drive, MEB Room 2110 Salt Lake City, UT 84112, USA*
[*] *jordan.gerton@utah.edu*

Supplement DOI: https://doi.org/10.6084/m9.figshare.24125583

Parent Article DOI: https://doi.org/10.1364/OE.499929

Simultaneous Spectral Differentiation of Multiple Fluorophores in Super-resolution Imaging Using a Glass Phase Plate: supplemental document

1. Phase Plate Fabrication

The phase plates were manufactured using plasma-enhanced chemical vapor deposition (PECVD). First, a layer AZ 9260 photoresist was spin-coated to a thickness of 10 microns on a cleaned boro-float glass wafer having a thickness of 1.1 mm. The photoresist was then photolithographically patterned for liftoff. PECVD via liftoff provides smoother surfaces than wet or reactive ion etching. Next, a layer of SiO_2 was deposited at 100 °C to a thickness of 960 nm on top of the substrate and was later lifted off in areas where the photoresist remained, by submerging it inchinchin acetone and applying ultrasonic power, revealing the smooth glass wafer surface. The wafer was then diced into individual chips. A chip was about 1x1 cm having a margin of about 2 mm around the deposition. The process is illustrated step by step in Fig. S 1.

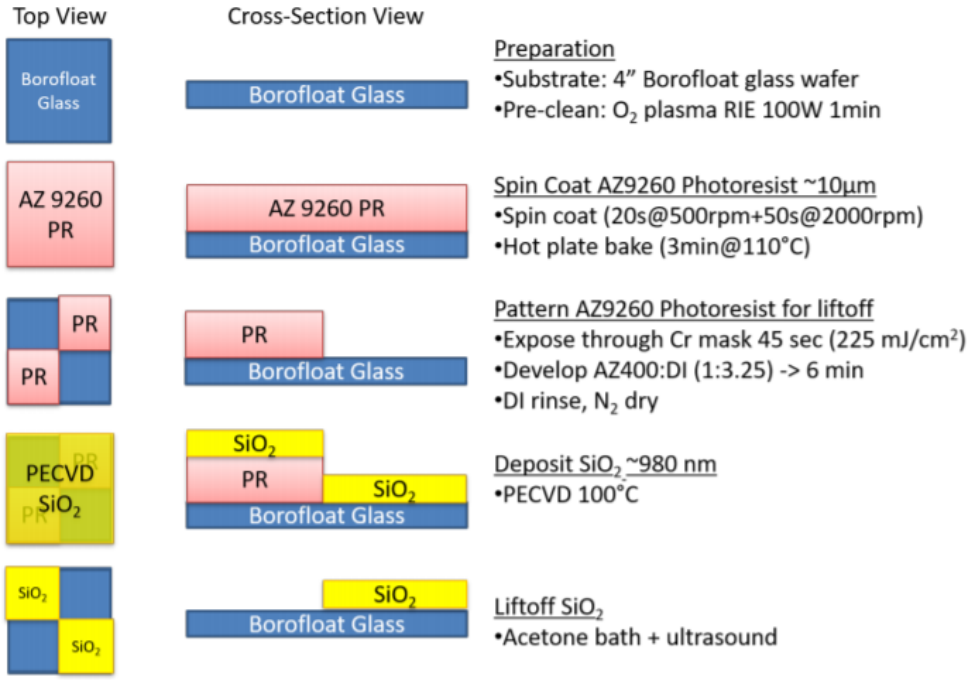

Fig. S 1 PECVD process flow. The left column shows the top view of the phase plate after each process step, the middle column shows the side view and the right column describes the process.

The phase plate mount shown in Fig. S 1 was 3D printed as an assembly of two circular caps with a smaller circular aperture at the center. Both the caps fit inside a 1-inch Thorlabs lens tube with very less wiggle space. One of the caps has a square groove at its center surrounding the aperture, to hold the phase plate at the center of the aperture. Once the phase plate sits inside the grooves of the cap, we close it with the other cap, mount it to a lens tube,module and secure it with a lens ring.

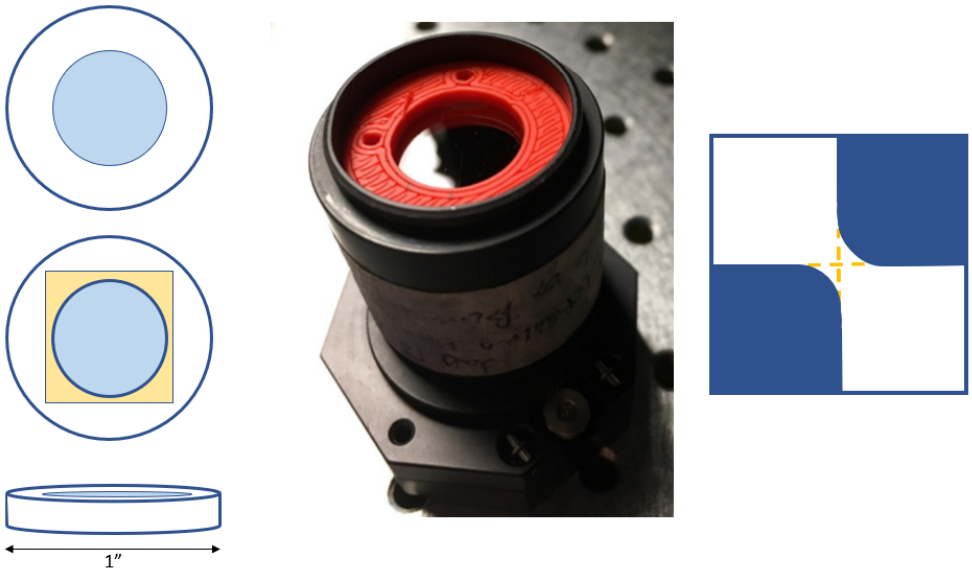

Fig. S 2 The 3D printed phase plate mount. The schematics on the left correspond to cap one and cap two when viewed from above and the side view of each cap from top to bottom. The blue regions indicate the apertures where light could pass through and the yellow region to the thin groove that secures the phase plate. The 3D printed caps are in orange in the actual image of the phase plate module in the center. A simplified drawing of the top-down view of the actual phase plate at its center is on the left. The blue area corresponds to the thick regions and the white to the nominal zero regions. The yellow dashed lines indicate the expected crossover.

2. Gibson-Lanni XPSF Model

The Gibson-Lanni XPSF model [1], [2] is described by the following set of equations. “XPSF” refers to the intensity at an arbitrary point (*x, y, z*) relative to the optical axis on the image recorded on camera for an XPSF corresponding to the wavenumber *k*. Let us define a cylindrical coordinate system by (ρ,θ,*z*). Then, following Born-Wolf interpretation and Gibson-Lanni simplification for Kirchhoff’s diffraction integral,

$$XPSF(x,y,z,k) = \left| Ak \int_0^1 \int_0^{2\pi} U(x,y,z,\rho,\theta)\, \rho\, d\rho\, d\theta \right|^2 \qquad \text{Eq S 1}$$

$$D \equiv (x,y,z,\rho,\theta)$$

$$U(x,y,z,\rho,\theta) = exp\left(\left(ik(n_a - n_p)\theta_p(D) + ik\theta_z(D) + i\psi_{GL}(D)\right)\right)$$

$$\psi_{GL}(D) = k\Delta_t n_i \sqrt{1 - \left(\frac{NA\,\rho}{n_i}\right)^2} + kz_p n_s \sqrt{1 - \left(\frac{NA\,\rho}{n_s}\right)^2} + \frac{NA\,\rho}{M}\sqrt{(x-x_0)^2 + (y-y_0)^2}\cos\left(\theta - \tan^{-1}\left(\frac{x-x_0}{y-y_0}\right)\right).$$

The terms in Eq S1 are described in Table S 1. If we were to adapt this model to a biplane or a multiplane imaging system, we need to add a defocus term as described by Kirshner et al [1] for the XPSFs corresponding to other planes, given by, $k\left(\frac{NA}{M}\right)^2 \Delta_z$, in which Δ_z is the axial displacement of the nth plane to the focused plane.

Table S 1 The terms used in equations for the Gibson-Lanni XPSF

Term	Description

x_0, y_0	Lateral coordinates of an emitter in the sample domain
NA	Numerical aperture of the objective/imaging system
n_i	Refractive index of the immersion medium
n_s	Refractive index of the sample
n_a	Refractive index of air (or else the refractive index of one of the diagonals of the phase plate)
n_p	Refractive index of glass (or else the refractive index of one of the diagonals of the phase plate)
M	Magnification of the microscope
Δ_t	Sample stage displacement with respect to the working distance of the objective
A	Normalization constant such that the integral is unity
Θ_p	Thickness profile of the phase plate
Θ_z	Weighted sum of Zernike aberrations

Since we place the phase plate at the Fourier plane of the collection path, a collimated bundle of rays would be incident on the phase plate for every emitter at the focal plane. Then, considering the geometry of the phase plate, the path difference incurred by the phase plate is $w = \frac{n_p \Theta_p}{\cos \alpha_1} - \frac{n_a \Theta_p}{\cos \alpha_2}$ where α_1 and α_2 are the angles that the light rays would make with the horizontal axis at the glass-air interface. However, for our imaging system, α_1 and α_2 are very small (< 10°), and thus, $w \approx (n_a - n_p)\Theta_p$ with a phase error of < 2%. For emitters away from the focal plane, the light rays incident on the phase plate are no longer collimated. However, for our system with light beams making small angles at the phase plate, the above approximation still produces a sufficiently accurate model for the off-plane XPSFs, facilitating z localizability as well.

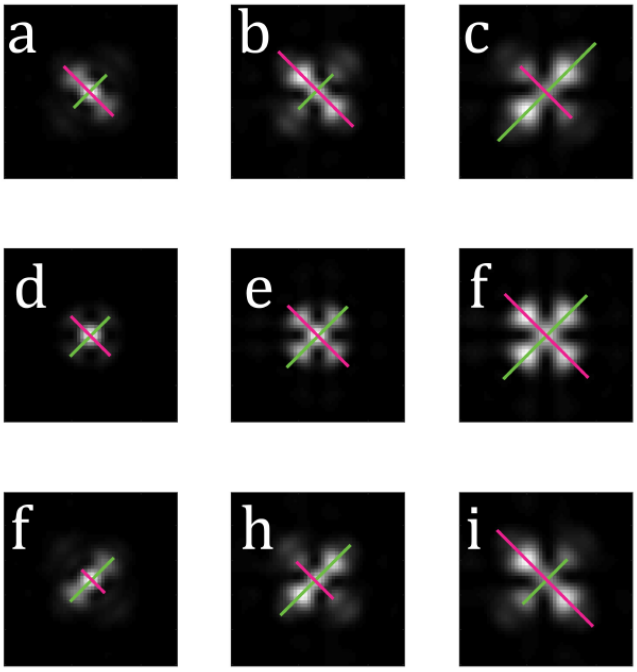

Fig. S 3 Simulated X-PSFs at different focal depths (rows) and spectra (columns). a) XPSF for a green channel at -300 nm. As the simulated emitter moves in focus, panel (d), and then above the focus, panel (f) (+300 nm), the PSF moves in toward its center along the magenta line and out away from its center along the green line. Panels (b), (e), and (h) show a similar behavior but more of the PSF is confined to the four outer-lobes, because this PSF was calculated for the orange channel. Finally, panels (c), (f), and (i) show the same basic behavior, however the direction of the ”tilt” left or right of the PSF out-of-focus is opposite to that of the other two spectral channels. This is

not always the case and depends on the thickness of the X-Phase plate step, which for this simulation was 640 nm.

The behavior of the XPSF family is illustrated using simulated PSFs in Fig. S 3 and thus explains the name “XPSF”; The intensity of the XPSFs move along the diagonals for out of focus emitters, making the shape of the letter ‘X’. For the 960 nm phase plate used for biological imaging, the direction of the “tilt” changed when moving from above and below focal plane emitters was the same for all emitters. The choice of the thickness of the phase plate may depend on the wavelengths of the emission spectra. We chose 960 nm so that the red and the green dyes we used had PSFs close to the two canonical shapes (described in the main manuscript).

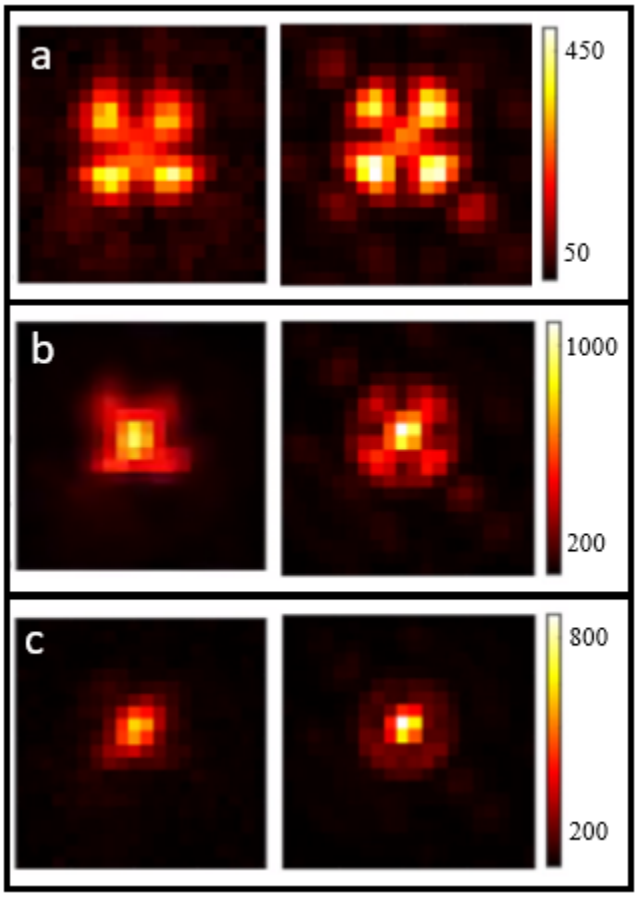

Fig. S 4 Data and Model for the XPSFs at focus. a) Red b) Orange c) Green XPSFs; Data on the left and the model on the right

Engineered PSFs often are largely dispersed in space with a large amount of the mass (intensity) of the PSF away from the center of the PSF. This may sometimes be a disadvantage when imaging multiple probes simultaneously, imaging a densely labeled sample, when there is a large background in the sample, when the photon budget is very limited, or when selecting the ROIs computationally. We obtained the radial sum of the XPSF and the Airy PSF to compare how the mass of the XPSF dispersed with the emission spectra and the depth. For this, we created the PSFs for our camera pixels and interpolated those PSFs over a grid of 100x100 pixels. Then, we obtained the sum of their mass in concentric circles starting from the center of the PSF at intervals corresponding to a single pixel (Orca Fusion-BT camera with 6.5-micron pixels) and obtained sums as shown in Fig. S 5 a) and b). We fitted a spline interpolant to the data points for continuity. Considering where 80% of the mass of the PSFs is contained, we calculate the dispersion (expansion) of the XPSF is only 30% (around 1 pixel radial expansion) when compared to a

corresponding Airy PSF for the emitters near the focal plane and less than 1% for emitters away from the focal plane. We identify this as a positive trait of the XPSF when imaging multiple probes simultaneously as the level of overlap when compared to Airy PSFs is not significantly large. The sum at each sector is shown in Fig. S 5 c) and d). There is a difference of about 2 camera pixels between the segments where the largest PSF mass occurs between the Airy PSF and the XPSF near the focal plane and almost no difference when away from the focal plane.

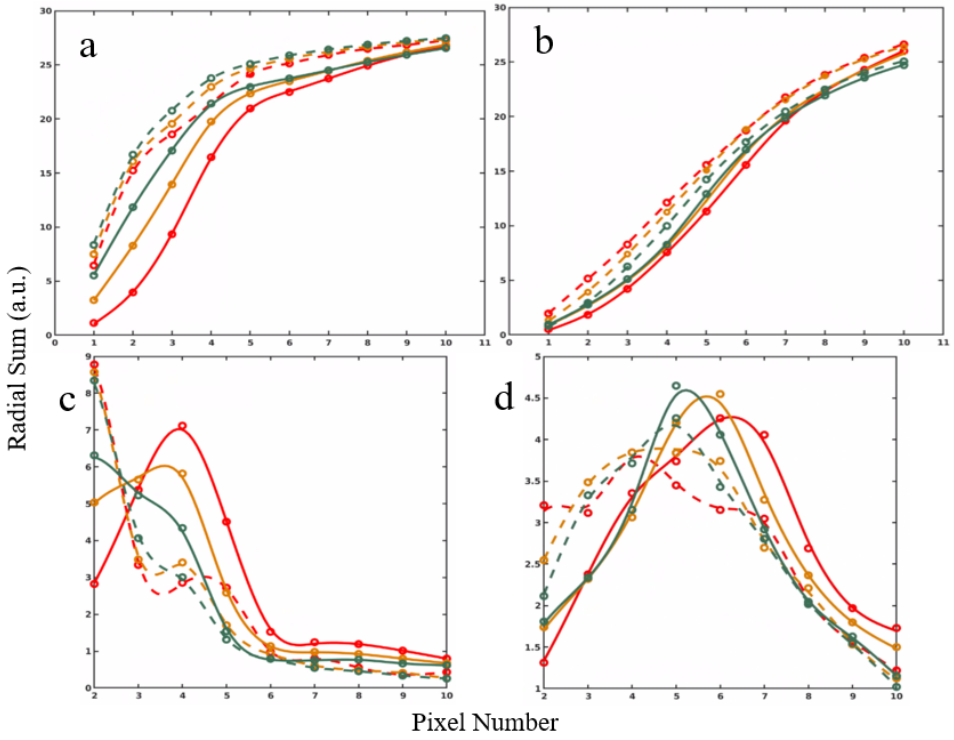

Fig. S 5 The intensity dispersion of the XPSFs compared to the Airy PSF. The cumulative radial sum of the intensity (mass) by considering increments of one pixel for the XPSF and the Airy PSF a) at z = 0 b) at z = 500 nm. The circular sector-wise sum c) at z = 0 d) at z = 500 nm. The solid lines correspond to the XPSF and the dashed lines to the Airy PSF. Red, orange, and green correspond to 680, 580, and 515 nm peak emissions for the three Tetraspeck bead spectra.

Fig. S 6 shows the truth table corresponding to the control experiment described in the Discussion Section of the manuscript and Fig.S6b shows the truth table obtained through Monte-Carlo simulations at around 100 photons per pixel background for a similar distribution of the number of PSF photons in a sample. The truth table for the control experiment shows that the PSFs belonging to AXF 488 have an increased chance of getting misidentified as that of CF 568 than predicted by the simulations

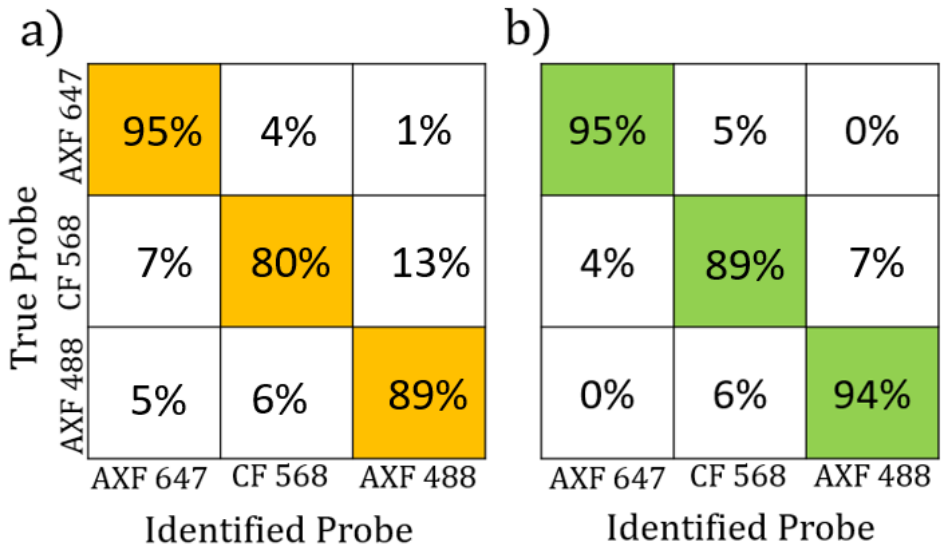

Fig. S 6 Truth tables describing the expected and the obtained spectral discernibility of the XPSFs. The truth table corresponding to the observed results of the control experiment is in panel a) and the results of the Monte-Carlo simulations for the best-case scenario described in the Discussion Section of the main manuscript is in panel b). The background is around 100 photons per pixel and the mean number of PSF photons is around 2500 photons per PSF. The diagonals in the truth tables correspond to the percentage of correct identifications for each probe.

[1] H. Kirshner, F. Aguet, D. Sage, and M. Unser, "3-D PSF fitting for fluorescence microscopy: implementation and localization application: 3-D PSF FITTING FOR FLUORESCENCE MICROSCOPY," *J. Microsc.*, vol. 249, no. 1, pp. 13–25, Jan. 2013, doi: 10.1111/j.1365-2818.2012.03675.x.

[2] M. Born and E. Wolf, *Principles of optics: electromagnetic theory of propagation, interference and diffraction of light*, 6th ed. Oxford ; New York: Pergamon Press, 1980. [Online]. Available: http://cdn.preterhuman.net/texts/science_and_technology/physics/Optics/Principles%20of%20Optics%20-%20M.Born,%20E.%20Wolf.pdf